Statistical 3D Prostate Imaging Atlas Construction via Anatomically Constrained Registration

Mirabela Rusu[a], B. Nicolas Bloch[b], Carl C. Jaffe[b], Neil M. Rofsky[c], Elizabeth M. Genega[d], Ernest Feleppa[e], Robert E. Lenkinski[c], and Anant Madabhushi[a]

[a]Case Western Research University, Cleveland, OH; [b]Boston University School of Medicine, Boston, Massachusetts; [c]UT Southwestern Medical Center, Dallas, Texas; [d]Beth Israel Deaconess Medical Center, Boston, Massachusetts; [e]Riverside Research Institute.

ABSTRACT

Statistical imaging atlases allow for integration of information from multiple patient studies collected across different image scales and modalities, such as multi-parametric (MP) MRI and histology, providing population statistics regarding a specific pathology within a single canonical representation. Such atlases are particularly valuable in the identification and validation of meaningful imaging signatures for disease characterization *in vivo* within a population. Despite the high incidence of prostate cancer, an imaging atlas focused on different anatomic structures of the prostate, i.e. an anatomic atlas, has yet to be constructed. In this work we introduce a novel framework for MRI atlas construction that uses an iterative, anatomically constrained registration (AnCoR) scheme to enable the proper alignment of the prostate (Pr) and central gland (CG) boundaries. Our current implementation uses endorectal, 1.5T or 3T, T2-weighted MRI from 51 patients with biopsy confirmed cancer; however, the prostate atlas is seamlessly extensible to include additional MRI parameters. In our cohort, radical prostatectomy is performed following MP-MR image acquisition; thus ground truth annotations for prostate cancer are available from the histological specimens. Once mapped onto MP-MRI through elastic registration of histological slices to corresponding T2-w MRI slices, the annotations are utilized by the AnCoR framework to characterize the 3D statistical distribution of cancer per anatomic structure. Such distributions are useful for guiding biopsies toward regions of higher cancer likelihood and understanding imaging profiles for disease extent *in vivo*. We evaluate our approach via the Dice similarity coefficient (DSC) for different anatomic structures (delineated by expert radiologists): Pr, CG and peripheral zone (PZ). The AnCoR-based atlas had a CG DSC of 90.36%, and Pr DSC of 89.37%. Moreover, we evaluated the deviation of anatomic landmarks, the urethra and veromontanum, and found 3.64 mm and respectively 4.31 mm. Alternative strategies that use only the T2-w MRI or the prostate surface to drive the registration were implemented as comparative approaches. The AnCoR framework outperformed the alternative strategies by providing the lowest landmark deviations.

Keywords: anatomic atlas, prostate, prostate cancer, 3D distribution, imaging signature in vivo, probabilistic atlas, image guided biopsy, histology ground truth for cancer

1. INTRODUCTION

Population-based descriptions of organ anatomy and pathology are constructed as statistical atlases by integrating information from multiple patients into a single canonical, 3D representation.[1,2] Imaging atlases are particularly valuable as they integrate multi-modal data, including non-invasive radiologic imaging such as multi-parametric (MP) MRI or histological specimens with disease annotation.

Anatomic atlases have been constructed for various organs including the lung,[3] heart,[4] and brain.[1,2] Despite the high incidence of prostate cancer (CaP),[5] an atlas capturing the different anatomic structures of the prostate (Pr), i.e. a 3D anatomic atlas, has, to the best of our knowledge, not yet been proposed. Such an atlas is essential as anatomic structures of the prostate can vary significantly in appearance on MRI. Anatomically, the prostate is divided into three zones: the central, transitional and peripheral zones. As the separation between the central and transitional zones is not visible on MRI, we consider them a unique anatomic region known as the central gland (CG). The peripheral zone (PZ) appears hyperintense on MRI while the CG and tumor appears

Corresponding author: Anant Madabhushi; E-mail: anant.madabhushi@case.edu; Telephone: +1 216 368 8519

hypointense. Furthermore, it has been showed[6] that CaP can have different MRI profiles on multi-parameteric (MP) MRI depending on the anatomic location of the pathology within the prostate[7] hence, prostate atlases should maintain separation of the anatomic structures.

Various authors[8–11] have attempted to generate a cancer probability atlas using a prostate surface registration on histological data. Yet, no anatomic constraints were considered and the cancer probability was defined on the *ex vivo* data. The excision of the prostate induces additional artifacts through fixation and the lack of adjacent anatomical constraints limits the usefulness of such atlases for *in vivo* imaging data.

Similarly, Betrouni et. al. used surface registration to constrain the CG and PZ in building a region-based model of the prostate.[12] In the latter paper, the MRI intensity of the anatomic structures is treated as a constant and is estimated as an average of MRI intensities, thus neglecting the information from the individual pixels. Martin et. al.[13] defined a probabilistic atlas of the prostate for automatic segmentation on T2-w MRI, yet distinction is not made between the different anatomic regions.

2. BRIEF OVERVIEW

In this work we introduce an iterative, constrained registration (AnCoR) scheme for the construction of a population-based atlas of the anatomic structures of the prostate. Moreover, the approach allows us to characterize the CaP spatial distribution. The MP-MRI data considered in our study was collected prior to radical prostatectomy. Also *ex vivo* histological specimens with ground truth CaP annotations are available from 23 subjects. Histology-MRI fusion allowed the mapping of the cancer annotation to MP-MRI.[14] While not explicitly addressed in this work, the precise mapping of tumor extent onto preoperative imaging and the resulting imaging atlas will allow for determination of imaging markers for CaP appearance *in vivo*.[6]

Although atlases are often used for segmentation[13] of the prostate, the newly presented prostate atlas serves to characterize 3D spatial extent of cancer within different spatial regions in the prostate. Previous prostate atlases[8–12] either ignore image intensities or lack anatomic constraints and therefore are *not* true anatomic atlases. Unlike previous work[15] that defined a 2D distribution, our cancer probability distribution characterizes the 3D spatial location of cancer and explicitly considers multiple anatomic regions.

The remainder of the paper is organized as following. First we discuss the novel contributions of this paper. Then follows the materials and methods section, where the methodology of the AnCoR framework is described along with the metrics used to evaluate the atlas framework. In our results section we provide quantitative evaluation of the prostate imaging atlas and the 3D extent of the cancer located within the volume. The article concludes with a discussion of the findings in the context of image-guided biopsy and future directions.

3. NOVEL CONTRIBUTIONS

Our work brings the following novel contributions:

1. To our knowledge, the anatomic prostate atlas presented in this paper is the first of its kind, in that the anatomy of the prostatic zones are explicitly considered in an MRI atlas.

2. In order to model the anatomic constraints, we implemented and identified optimal parameters for a novel scoring function that incorporates both MRI intensity and a regularization constraint on the surface of anatomic regions.

3. The atlas allows for resolvability of the spatial distribution of cancer relative to the anatomic structures in the prostate.

4. METHODS

4.1 Atlas building framework

The anatomic constrained registration (AnCoR) framework uses an iterative procedure that progressively updates the atlas as the datasets become more accurately aligned. The procedure starts with simple centering of the individual glands and are finalized by a deformable registration (Figure 1). As the various steps are executed, different performance metrics are used to assess the accuracy of the registration (Section 5.5). A summary of the notations and abbreviations used in this paper are presented in Table 1.

Symbol	Definition
$\mathcal{A}_A$	Atlas construction through AnCoR framework
$\mathcal{A}_I$	Atlas construction through MRI intensity registration
$\mathcal{A}$	Reference template in registration
$\mathcal{X}$	Subject dataset
$\mathcal{X}^{\mathbf{T}}$	X with applied transform $\mathbf{T}$
ψ	Scoring function
ψ_S	Surface term of the scoring function
ψ_I	Image intensity term of the scoring function
I_2	Mutual information (MI)
w	weight of the surface misalignment terms

Table 1. Symbols and notations employed in this paper.

4.2 Inter-subject Registration

Inter-subject registration is at the core of the framework and ensures that a subject's imaging dataset is aligned to the reference template, which can be either another subject's dataset, or, as presented here, the statistical atlas representing an average of multiple datasets. In general, a registration technique seeks to identify the transformation that aligns two datasets $\mathcal{A}$ and $\mathcal{X}$ while optimizing a cost function ψ. Hence, the optimal transformation is calculated as

$$\mathbf{T}_{\max} = \arg\max_{\mathbf{T}} \psi(\mathcal{A}, \mathcal{X}^{\mathbf{T}})$$

where $\mathcal{X}^{\mathbf{T}}$ represents the transformed image of the dataset $\mathcal{X}$, $\mathcal{A}$ is the reference template and ψ quantifies the similarity between the $\mathcal{A}$ and $\mathcal{X}^{\mathbf{T}}$. In the AnCoR framework, the transform $\mathbf{T}$ progressively encodes more complex transformations, ranging from centering and scaling to deformable transformation.

In general, an affine transform is defined by 9 parameters representing the 3D translation, 3D rotation and 3D scaling. Centering and scaling, which are particular cases of affine transformations are applied first; this is followed by a general affine transformation. Moreover, free form deformation (FFD)[16] is employed to elastically align the datasets subsequent to the affine transformation step. FFD optimizes the location of control points that are initially distributed uniformly on a 3D grid, while 3D B-splines are used to interpolate between these control points.

4.3 Modeling Anatomic Constraints

The cost function optimized by the AnCoR framework incorporates an image intensity similarity term and surface alignment term

$$\psi(\mathcal{A}, \mathcal{X}) = \psi_I(\mathcal{A}, \mathcal{X}) + \sum_{r=1}^{n} w_r \cdot \psi_S^r(\mathcal{A}, \mathcal{X}),$$

where $\psi_I(\mathcal{A}, \mathcal{X})$ assesses the similarity of image intensities between $\mathcal{A}$ and $\mathcal{X}$ while $\psi_S^i(\mathcal{A}, \mathcal{X})$ quantifies the alignment of the anatomic structure $r = 1..n$ in the datasets $\mathcal{A}$ and $\mathcal{X}$, and w_r is the empirical weight of the anatomic structure r. In this work, we consider $n = 2$ anatomic regions, the Pr and CG. More specifically ψ_S may also be estimated based on the mean squared error:

$$\psi_S(\mathcal{A}, \mathcal{X}) = -\frac{1}{N} \cdot \sum_{c \in \mathcal{C}} [\mathcal{A}(c) - \mathcal{X}(c)]^2$$

where N is the number of voxels, and c represents the cth voxel of the grid $\mathcal{C}$ in the volume $\mathcal{A}, \mathcal{X}$. The goal of the metric is to maximize the image intensity while maximizing the alignment of the anatomic structures.

The AnCoR framework is developed as an iterative registration procedure comprised of several steps (Figure 1):

1. *Segmentation* of anatomic structures (Pr, CG, PZ, vrethra and verumontanum) was done by an expert radiologist based on the T2-w MRI while the cancer extend was delineated by an expert pathologist on the H&E stained histology slices.

2. *Preprocessing* of the image intensities is performed to remove bias field artifacts[17] and outliers in MRI intensity.

3. *Create atlas* by centering and scaling all subjects in the cohort. The centering was performed to bring all datasets to a common center, while the scaling was needed to correct for the large variations in Pr size in the population. For the scaling, the volume of the bounding box surrounding the prostate was computed and restrained to a constant $90cm^3$ which is a reasonable upper bound of maximal prostate sizes, and an identical scaling factor was applied on the X, Y and Z axes.

   This simple affine transform is performed to bring all datasets into a common reference frame without performing a registration to a particular subject, which may potentially bias the reference. This initial transformation allows for the creation of a first reference template by averaging all datasets in the cohort and thereby generating an initial approximate statistical atlas.

4. *Affine registration with anatomic constraints* is then performed between the datasets in the cohort and the reference template obtained during the previous step. Datasets in the cohort are averaged following affine registration to create the new reference template and an updated statistical atlas.

5. *The deformable registration* attempts to elastically align the different anatomic regions. Similarly to the previous step, the statistical atlas is updated by averaging the aligned datasets.

6. *Anatomic structure and landmarks, other than the constrained terms,* are updated with each additional optimized transformation.

5. EXPERIMENTAL DESIGN

The AnCoR framework is applied to create an anatomic statistical atlas of the prostate, in which we constrain Pr and CG, and use the anatomic structures (Pr, CG and PZ) and anatomic landmarks (urethra, verumontanum) to evaluate the performance of the atlas building framework.

5.1 Data

The current atlas was built based on endorectal T2-w MRI from 51 subjects with biopsy confirmed CaP diagnosis; however, the prostate atlas is seamlessly extensible to include additional modalities, such as dynamic contrast enhanced MRI. The datasets have $M' \times M' \times M$ voxels, where $M' \in \{400, 512\}$ and M ranges between 32 and 56, with dimensions of 0.27-0.40 mm in the XY plane and 2.2-3.0 mm in the Z plane. The datasets were collected at two different institutions, at 1.5 Tesla for 7 subjects and 3.0 Tesla for the remaining 43 subjects. Figure 1 shows the MRI from different subjects, for which the CG, Pr and CaP are highlighted. The illustrated datasets are representative of the natural variation of the prostate in the cohort in terms of gland size, shape, and MRI intensity in the different anatomic regions.

An expert radiologist manually annotated the Pr, CG and PZ for 51 patients, as well as the urethra and verumontanum for 11 subjects. The annotations were done based on the T2-w MRI using 3D Slicer.[18]

5.2 Mapping CaP from histology onto MRI

The cancer extent was delineated by an expert pathologist on digitalized *ex vivo* whole mount sections from 23 patient studies. The CaP delineation was then mapped through the registration of histology slices and MRI using an approach originally introduced by Chappelow et al.[14] The latter used deformable registration based on B-splines in order to register corresponding histological 2D images and the MRI slices in which the prostate was segmented. Such correspondences were obtained from an expert radiologist by judicious inspection of two different data types for similar anatomic landmarks. For instance, anatomic feature such as the location of the urethra/veromontanum or benign prostatic hyperplasia (BPH) were considered. In the next step, the segmented prostates from both MRI and histology are automatically aligned using free form deformation (FFD)[16] with MI as a scoring function.
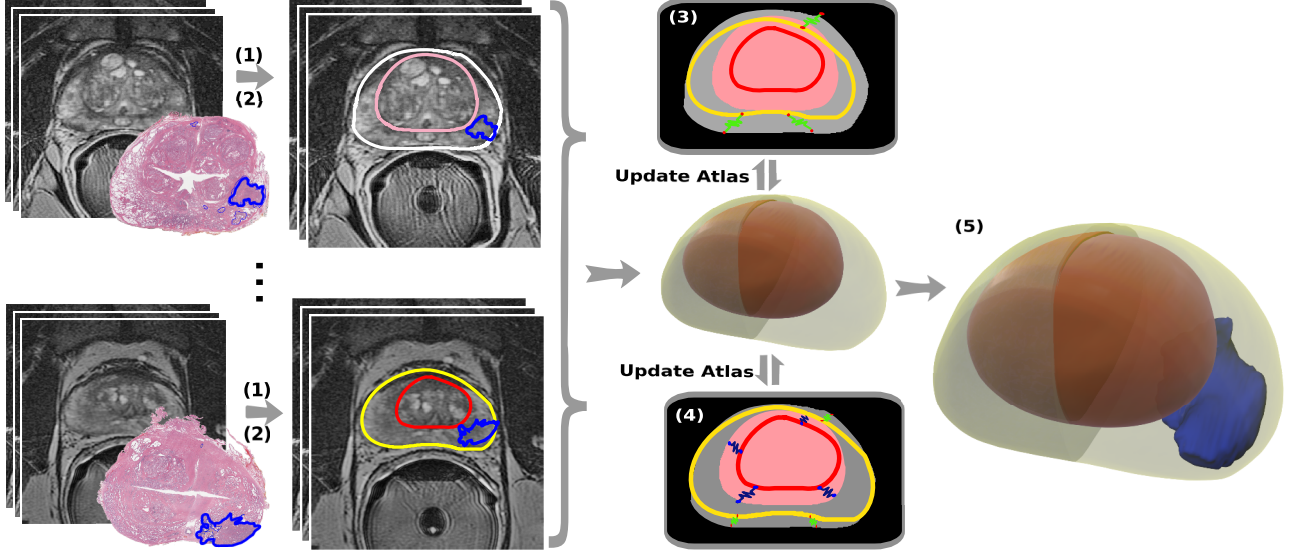
Figure 1. AnCoR Flowchart. **(1)** Manually segment anatomic regions: prostate (white, yellow), and central gland (red, pink); **(2)** Map cancer (blue) from histology to MP-MRI[14] ; **(3)** Perform affine registration constraining Pr and CG boundaries; **(4)** Update atlas by averaging T2-w MRI from (3) and use as registration fixed image; perform FFD registration, constraining both Pr and CG using equal weights; **(5)** Identify cancer spatial distribution.

5.3 AnCoR framework for the construction of the prostate atlas

The scoring function ψ is defined as

$$\psi(\mathcal{A}, \mathcal{X}) = I_2(\mathcal{A}, \mathcal{X}) + w \cdot \psi_S^{CG}(\mathcal{A}, \mathcal{X}) + w \cdot \psi_S^{Pr}(\mathcal{A}, \mathcal{X}),$$

where $\mathcal{X}$ represents the 3D T2-w MRI of the subject while $\mathcal{A}$ represents the reference template, i.e. the altas constructed at the previous step. In this current work, we choose MI to assess the MRI intensity similarity and mean squared error (MSE) to evaluate the surface alignment. We set $w_{CG} = w_{Pr} = w$ to ensure an equal influence of the surface boundary terms. This choice was made through empirical testing that suggested that having differential weights was not necessary.

5.4 Experimental strategy

Table 2 summarizes the experiments performed here. The framework was used to build $\mathcal{A}_I$ by setting $w = 0$ to enable the registration based solely on T2-w MRI intensities (Experiment E1). Such experiment was considered as a comparative strategy to test whether a combination of intensity and surface constrains in needed. Moreover, as part of the experiment E1, we also compute the spatial extend of the CaP within the population.

In experiment E2, the AnCoR framework was employed to construct $\mathcal{A}_A$ where both MRI intensity and surface constraints are optimally weighted through the exploration of the parameter range in a sub-cohort(data not shown).

Experiment		Cohort size	Description
E1.	$\mathcal{A}_A$	51	Pr, Cg, PZ annotations
		23	Ground truth CaP annotation from H&E slices
E2.	$\mathcal{A}_I$	51	Pr, Cg, PZ annotations

Table 2. Subject cohorts used for the different experiments).

5.5 Evaluation measures

The constructed atlases, $\mathcal{A}_A$ and $\mathcal{A}_I$, are evaluated through two performance metrics, the deviation between landmarks and overlap between anatomic regions. As the core component of the atlas construction is inter-subject registration, our metrics are estimated on landmarks and regions that are consistently discernible across different subjects. Benign prostatic hyperplasia (BPH) nodules and calcification are typically used as landmarks for intra-subject registration. However these are usually not consistent between different subjects and thus cannot be employed here. Thus we choose the urethra and verumontanum as landmarks, and we expect that these landmarks will be well aligned in $\mathcal{A}_A$. Note that the urethra shows up as a tubular curved shape that crosses the prostate from base to apex while the verumontanum has a v-like shape visible on a few axial slices that are located in mid-gland.

In order to compute the deviation between these anatomical landmarks, the 3D medial axes[19] were first computed and then the deviation between the medial axis points was estimated. The medial axis is defined on a per slice basis, as the points at the interior of the annotated region, furthest away from the surface. For two subjects $\mathcal{X}_1$ and $\mathcal{X}_2$, we estimated the deviation $||M_1, M_2||$ of their medial axes M_1 and M_2 as the average Euclidean distance between axial proximal points. The point $P_i \in M_1$ is considered proximal to $P_j \in M(X_2)$ if $||P_i, P_j||_2 < ||P_i, P_k||_2$ where P_k is any point in M_2 where $j \neq k$. Note, that if P_i is considered proximal to P_j it does not imply that P_j is proximal to P_i. Thus, we estimate the deviation between the anatomic landmarks, either the urethra or the verumontanum, of the subject $\mathcal{X}_1$ and $\mathcal{X}_2$ as

$$||\mathcal{X}_1, \mathcal{X}_2|| = \frac{1}{2} \cdot (||M_1, M_2|| + ||M_2, M_1||),$$

The average deviation of the landmark within the cohort is estimated following each registration step as the averaged inter-subject deviations for any possible pair-wise combination. For the n subjects $\mathcal{X}_1, \ldots, \mathcal{X}_n$:

$$||\mathcal{X}_1, \ldots, \mathcal{X}_n|| = \frac{1}{(n-1)(n-2)} \cdot \sum_{s_1 \neq s_2} \sum ||X_{s_1}, X_{s_2}||,$$

The Dice similarity coefficient (DSC) estimate the degree of overlap between two masks: $DSC(\mathcal{X}_1, \mathcal{X}_2) = \frac{2 \times |X_1 \cap X_2|}{|X_1| + |X_2|}$, where $|\mathcal{X}|$ represents the cardinality of set $\mathcal{X}$.

To estimate the degree of overlap following the registration step, we computed the averaged DSC between the subjects $\mathcal{X}_i$, $i = 1..n$ and the reference template $\mathcal{A}$ as

$$DSC(\mathcal{X}_1, \ldots, \mathcal{X}_n) = \frac{1}{n} \sum_{i=1}^{n} DSC(\mathcal{X}_i, \mathcal{A}),$$

The DSC is quantified from the binary mask of each anatomic region relative to the reference template $\mathcal{A}$ for Pr, CG and PZ.

The scheme to build the atlas was implemented using the ITK framework[20] and an evolutionary optimizer. The cohort of 11 subjects with landmark annotations was utilized to perform an exhaustive exploration of the parameter space (data not shown). Following this parameterization step, we choose $w = 0.5$ for the affine stage, which allows for the contribution of the surfaces to be weighted significantly higher compared to just the image intensities. It was found that the value of $w = 0.05$ yielded a reasonable tradeoff between landmark deviation and optimal overlap for the deformable registration step.

6. EXPERIMENTAL RESULTS AND DISCUSSION

6.1 Experiment E1: AnCoR Atlas

The AnCoR Atlas $\mathcal{A}_A$ is constructed based on the 51 subject cohort. Figures 2(d)-2(f) show the sections in $\mathcal{A}_A$ at the level of the prostate base. As expected, hypointense regions are observable in CG, while the PZ shows as a hyperintense region. The outline of the urethra is more obviously discernible as well particularly in the midgland
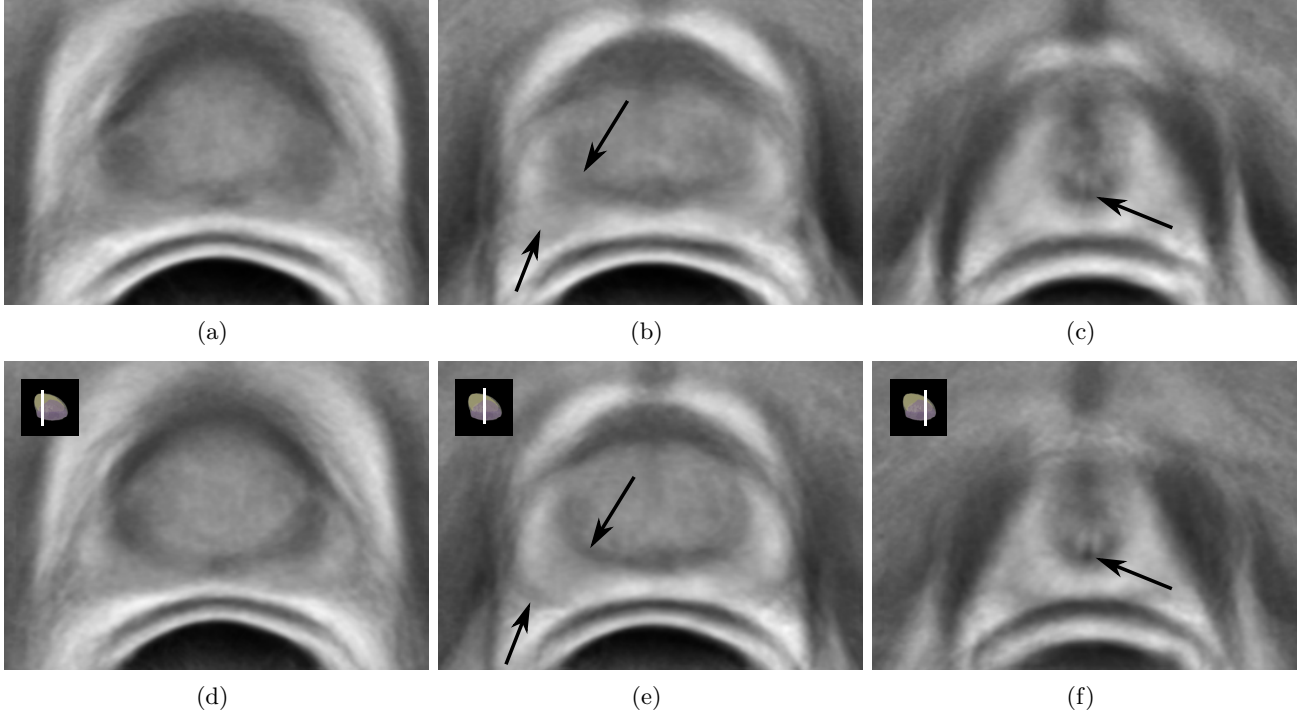
Figure 2. Intensity statistical atlas as obtained in (a)-(c) $\mathcal{A}_I$, T2-w MRI intensity based registration *without* Pr and CG constraints; (d)-(f) $\mathcal{A}_A$, AnCoR framework with equal contributions from CG and Pr; (a), (d) base; (b), (e) midgland region; (c), (f) apex. The CG and Pr boundaries are more readily identifiable in $\mathcal{A}_A$ compared to $\mathcal{A}_I$ (see arrows in (b) and (e)). Moreover, the urethra is more clearly discernible in $\mathcal{A}_A$ relative to $\mathcal{A}_I$ (see arrow in (c) and (f)).

and apex regions. Moreover, $\mathcal{A}_A$ also includes a statistical shape model for the Pr, CG and Pz as indicated in Figures 3.

The spacial distribution of cancer was estimated from the 23 subjects for which we have radical prostatectomy specimens with annotated cancer. As expected, the highest frequency of cancer is present in the PZ rather close to the neurovascular bundles.[5] Yet, cancer is also often observed in CG towards the apex of the prostate (Figure 3). The distribution of cancer is not symmetric, as already observed by Donohue and Miller.[21]

We were able to build not only a shape atlas of the prostatic regions (Figure 3(a)) as described by Betrouni et. al.,[12] but also an MRI intensity atlas (Figures 2(d)-2(f)).

6.2 Experiment E2: Comparative strategies

As a comparative strategy, we also evaluated the outcome of our framework in $\mathcal{A}_I$, where $w = 0$ and only the T2-w MRI intensities drive the registration (Figure 2(a)-2(c)). As expected, the unconstrained atlas becomes misaligned with the different anatomic regions as quantified by the lower DSC values for each region (Table 3). Misalignment is also apparent qualitatively in Figure 2(b) when compared to Figure 2(e) (see arrows). Such misalignment can be observed as a blurring effect, especially visible at the CG and PZ boundary and at the region adjacent to the endorectal coil. Moreover such misalignments can also be visible close to the urethra as indicated by arrows in Figures 2(f) and 2(c).

7. CONCLUDING REMARKS

We presented a novel anatomic atlas of the prostate from multi-parametric MRI. In this implementation we constructed the atlas based on T2-w MRI, using an iterative registration scheme based on affine and elastic registration. The registration was developed to ensure the proper central gland (CG) alignment with the goal of generating an anatomically correct representation of the prostate. However, such an alignment of the CG

Atlas	DSC (%)					Deviation (mm)	
	Pr	CG	PZ	Seminal Vesicles	Neurovascular Bundles	Urethra	Veru-montanum
Preprocessing	78.49	69.32	54.57	29.57	23.56	5.84	8.47
$\mathcal{A}_I$	83.21	77.16	67.82	**37.24**	28.07	5.64	6.47
$\mathcal{A}_A$	**90.36**	**89.37**	**77.01**	33.31	**33.91**	**3.64**	**4.31**

Table 3. Evaluation of $\mathcal{A}_A$ and $\mathcal{A}_I$. DSC is shown as percentages, while deviations are measured in millimeters (mm). The lowest landmark deviations are observed in $\mathcal{A}_A$. The preprocessing step refers to the translation that aligns all MRI datasets at the geometric center of the prostate.

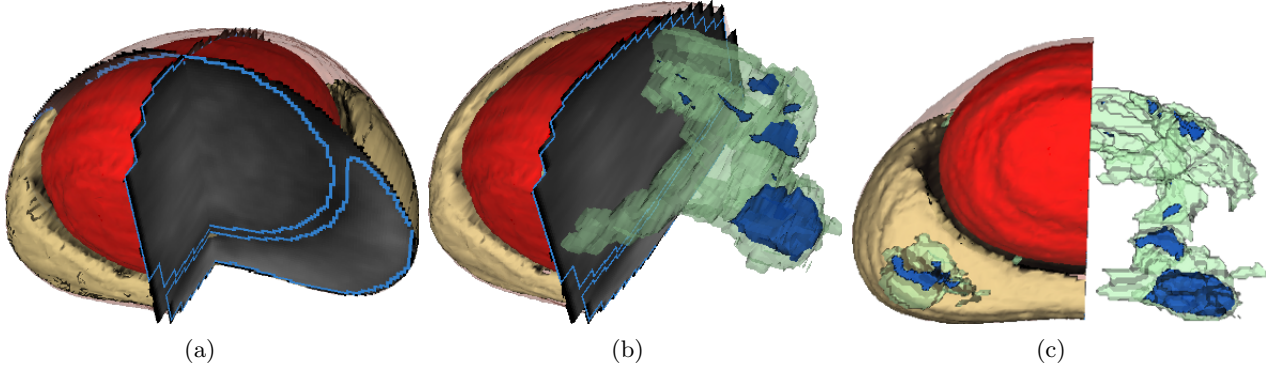(a)   (b)   (c)

Figure 3. (a) 3D representation of the AnCoR atlas $\mathcal{A}_A$; CG, PZ and Pr are outlined in red, yellow, and respectively transparent pink; (b)-(c) Cancer distribution in the prostate; Higher frequency of cancer is depicted in blue, while lower frequency are shown in green.

can only be achieved with anatomical constraints, suggesting the need for a novel anatomically constrained cost function to drive the registration. The atlas was built on a 51 subject cohort, from which only a subset (23 patients) had *ex vivo* histology specimens with cancer annotations that allowed us to characterize the distribution of cancer within the different anatomic regions of the prostate. A registration based on MRI intensity alone had difficulty aligning the anatomic regions as their boundaries are subtle, causing a blurring effect at the edges of the anatomic regions in Figure 2.

Furthermore, our AnCoR framework provides a platform for the fusion of multi-modal data into a single canonical representation. While not explicitly addressed in this work, the precise mapping of tumor extent onto preoperative imaging should also allow for determination of imaging markers for CaP appearance *in vivo* and might provide grounds for future localized treatment options. In fact this framework could be used to integrate multi-modal, multi-scale imaging and molecular data by including additional MP-MRI protocols and complementary proteomic and genomic marker information. Such a comprehensive atlas would allow for the identification and validation of *in vivo* imaging markers for aggressive disease based on co-expression with other molecular and histologic measurements. In the future, we plan to increase the cohort size to augment the statistical power of the atlas.

8. ACKNOWLEDGEMENTS

REFERENCES

[1] Evans, A., Collins, D., Mills, S., Brown, E., Kelly, R., and Peters, T., "3d statistical neuroanatomical models from 305 mri volumes," in [*Nuclear Science Symposium and Medical Imaging Conference, 1993., 1993 IEEE Conference Record.*], 1813 –1817 vol.3 (oct-6 nov 1993).

[2] Toga, A. W., Thompson, P. M., Mori, S., Amunts, K., and Zilles, K., "Towards multimodal atlases of the human brain.," *Nat. Rev. Neurosci.* **7**(12), 952–66 (2006).

[3] Li, B., Christensen, G. E., Hoffman, E. A., McLennan, G., and Reinhardt, J. M., "Establishing a Normative Atlas of the Human Lung: Intersubject Warping and Registration of Volumetric CT Images," *Academic Radiology* **10**(3), 255 – 265 (2003).

[4] Perperidis, D., Mohiaddin, R. H., and Rueckert, D., "Spatio-temporal free-form registration of cardiac MR image sequences," *Med. Image Anal.* **9**(5), 441 – 456 (2005).

[5] Fütterer, J. J. and Barentsz, J. O., "3T MRI of prostate cancer," *ApR* **38**, 25–32 (2009).

[6] Viswanath, S. E., Bloch, N. B., Chappelow, J. C., Toth, R., Rofsky, N. M., Genega, E. M., Lenkinski, R. E., and Madabhushi, A., "Central gland and peripheral zone prostate tumors have significantly different quantitative imaging signatures on 3 tesla endorectal, in vivo T2-weighted MR imagery," *J. Magn. Reson. Imaging* (2012).

[7] Akin, O., Sala, E., Moskowitz, C., Kuroiwa, K., Ishill, N., Pucar, D., Scardino, P., and Hricak, H., "Transition Zone Prostate Cancers: Features, Detection, Localization, and Staging at Endorectal MR Imaging," *Radiology* **239**(3), 784–792 (2006).

[8] Sofer, A., Zeng, J., and Mun, S., "Optimal biopsy protocols for prostate cancer," *Annals of Operations Research* **119**(1), 63–74 (2003).

[9] Shen, D., Lao, Z., Zeng, J., Zhang, W., Sesterhenn, I. A., Sun, L., Moul, J. W., Herskovits, E. H., Fichtinger, G., and Davatzikos, C., "Optimized prostate biopsy via a statistical atlas of cancer spatial distribution.," *Med. Image Anal.* **8**(2), 139–50 (2004).

[10] Zhan, Y., Shen, D., Zeng, J., Sun, L., Fichtinger, G., Moul, J., and Davatzikos, C., "Targeted prostate biopsy using statistical image analysis," *IEEE Trans. Pattern Anal. Mach. Intell.* **26**(6), 779–788 (2007).

[11] Ou, Y., Shen, D., Zeng, J., Sun, L., Moul, J., and Davatzikos, C., "Sampling the spatial patterns of cancer: Optimized biopsy procedures for estimating prostate cancer volume and gleason score," *Med. Image Anal.* **13**(4), 609 (2009).

[12] Betrouni, N., Iancu, A., Puech, P., Mordon, S., and Makni, N., "ProstAtlas: A digital morphologic atlas of the prostate.," *Eur. J. Radiol.* , 3–9 (2011).

[13] Martin, S., Troccaz, J., and Daanen, V., "Automated segmentation of the prostate in 3D MR images using a probabilistic atlas and a spatially constrained deformable model," *Med. Phys.* **37**(4), 1579 (2010).

[14] Chappelow, J., Bloch, B. N., Rofsky, N., Genega, E., Lenkinski, R., DeWolf, W., and Madabhushi, A., "Elastic registration of multimodal prostate MRI and histology via multiattribute combined mutual information," *Med. Phys.* **38**(4), 2005–18 (2011).

[15] Xiao, G., Bloch, B. N., Chappelow, J., Genega, E., Rofsky, N., Lenkinski, R., and Madabhushi, A., "A structural-functional MRI-based disease atlas: application to computer-aided-diagnosis of prostate cancer," in [*SPIE Medical Imaging*], **7623**(1) (2010).

[16] Lee, S., Wolberg, G., and Shin, S. Y., "Scattered data interpolation with multilevel B-splines," *IEEE TVCG* **3**(3), 228–244 (1997).

[17] Cohen, M. S., DuBois, R. M., and Zeineh, M. M., "Rapid and effective correction of RF inhomogeneity for high field magnetic resonance imaging," *Human Brain Mapping* **10**(4), 204–211 (2000).

[18] Pieper, S., Halle, M., and Kikinis, R., "3D Slicer," *IEEE International Symposium on Biomedical Imaging* , 632–635 (04 2004).

[19] Blum, H., "A Transformation for Extracting New Descriptors of Shape," in [*Models for the Perception of Speech and Visual Form*], 362–380 (1967).

[20] Yoo, T. S., Ackerman, M. J., Lorensen, W. E., Schroeder, W., Chalana, V., Aylward, S., Metaxas, D., and Whitaker, R., "Engineering and algorithm design for an image processing Api: a technical report on ITK–the Insight Toolkit.," *Stud. Health Technol. Inform.* **85**, 586–92 (2002).

[21] Donohue, R. E. and Miller, G. J., "Adenocarcinoma of the prostate: biopsy to whole mount. denver va experience.," *The Urologic clinics of North America* **18**(3), 449 (1991).